Effect of nonaxisymmetric magnetic perturbations on divertor heat and particle flux profiles in National Spherical Torus Experiment[a)]

J-W. Ahn,[1,b)] R. Maingi,[1] J. M. Canik,[1] A. G. McLean,[1] J. D. Lore,[1] J.-K. Park,[2]
V. A. Soukhanovskii,[3] T. K. Gray,[1] and A. L. Roquemore[2,]

[1]*Oak Ridge National Laboratory, Oak Ridge, Tennessee 37831, USA*
[2]*Princeton Plasma Physics Laboratory, Princeton, New Jersey 08543, USA*
[3]*Lawrence Livermore National Laboratory, Livermore, California 94551, USA*

Small, nonaxisymmetric magnetic perturbations generated by external coils have been found to break the axisymmetry of heat and particle flux deposition pattern in the divertor area in the National Spherical Torus Experiment (NSTX). This breaking by the applied 3-D field causes strike point splitting that is represented as local peaks and valleys in the divertor profiles. In case of $n = 3$ fields application, the broken toroidal symmetry of the divertor profile shows $120°$ of spatial periodicity while data for $n = 1$ fields provide a fully nonaxisymmetric heat and particle deposition. Field line tracing showed good agreement with the measured heat and particle flux profiles. Higher toroidal mode number ($n = 3$) of the applied perturbation produced more and finer striations in the divertor profiles than in the lower mode number ($n = 1$) case. Following the previous result of the intrinsic strike point splitting by the $n = 3$ error fields [Nucl. Fusion **50**, 045010 (2010); J. Nucl. Mater. (2011), doi:10.1016/j.jnucmat.2011.01.115], result of the connection length profile from field line tracing identifies intrinsic error field as a possible source of the intrinsic splitting. In determining the strike point splitting pattern, q_{95} is found to play an important role; higher q_{95} produces finer striations and induces higher fraction of heat flux to flow through the split strike point channels. Higher pedestal electron collisionality also made the striations in the D_α profile more pronounced in the given range of collisionality variation. The radial location of local peaks in the profiles during the triggered edge localized modes (ELMs) by the applied $n = 3$ fields stays similar before and after the application. This shows that the heat flux from the triggered ELMs follows the mode number of the applied perturbation. The external magnetic perturbation can reattach detached divertor plasma, but this can be overcome by detaching the plasma with additional divertor gas puffing. © *2011 American Institute of Physics*. [doi:10.1063/1.3574522]

I. INTRODUCTION

It was found that small, nonaxisymmetric magnetic field perturbations produced by internal or external coils can break the toroidal symmetry of divertor heat and particle deposition in tokamaks, generating striated heat and particle footprints at the divertor surface, e.g., in Compass-D,[1] DIII-D,[2–4] and National Spherical Torus Experiment (NSTX).[5] This is a direct consequence of the "strike point (SP) splitting" caused by the 3-D magnetic field perturbations to the plasma edge.[2] As many tokamak plasma facing components (PFCs) are designed and built assuming toroidal symmetry to protect areas where high heat and particle fluxes are expected from the 2-D equilibrium, these nonaxisymmetric, i.e., 3-D, divertor profiles could result in additional engineering constraints. These applied 3-D magnetic perturbations are also found to suppress[6] or mitigate[7] edge localized modes (ELMs) in conventional tokamaks, while they trigger ELMs in spherical tokamaks.[8,9] In NSTX, the 3-D field perturbation was applied to ELM-free H-mode plasmas achieved with lithium (Li) wall coatings of the plasma facing components,[10] in order to trigger controlled ELMs

with the goal of flushing impurities and reducing radiated power from the core plasma.[11] It is therefore important to investigate the effect of 3-D field on heat and particle flux profiles during and between ELMs and their relation to a wide range of plasma parameters.

II. EXPERIMENTAL SET-UP AND MEASUREMENT TECHNIQUE

The 3-D perturbation fields were generated with a set of six midplane coils, external but close-fitting to the vacuum vessel, that are typically used for error field correction and resistive wall mode feedback control.[12,13] The coils were configured to apply an $n = 3$ field in the ELM-destabilization experiments, with a generated magnetic perturbation at the separatrix, $\delta B/B \sim 0.5\%$ for the peak δB at the coil centre and in the order of 0.1% for the integrated δB over the coil surface. Another coil setting was also implemented to apply an $n = 1$ field with $\delta B/B \sim 0.3\%$ for the peak δB. The poloidal spectrum of the applied magnetic perturbation is broad at the plasma edge,[9] reaching high enough mode numbers to be resonant with high edge safety factor values ($q_{95} \sim 11$).

The heat flux measurement is made with an SBF-161 infrared (IR) camera.[14] The reference point of the toroidal angle is located at the centre of the midplane coil #1, positive

angle is measured counter-clockwise from the reference point [Fig. 1(b) in Ref. 15]. The IR camera is installed at the toroidal angle $\varphi = 135°$. The camera takes IR images of the lower divertor plates in 2-D with a temporal resolution of 1.6–6.3 kHz, depending on the frame size, and the spatial resolution of 5–7 mm. The camera measures surface IR emission, which passes through a newly installed dual band IR adaptor[16] to take a ratio between long wavelength (7–10 μm) and medium wavelength (4–6 μm) IR intensities. This ratio is converted to surface temperature from bench and *in situ* calibrations. A 2-D heat conduction code called THEODOR (Ref. 17) is used to calculate the divertor heat flux profile from the measured surface temperature. The two dimensions are radial and tile depth directions for tiles with finite thickness as well as taking account of temperature dependent material parameters. However, the effect of Li coatings on the surface emissivity has not been properly assessed for the data presented in this paper, because the condition of Li coated surfaces varies with plasma conditions, and the surface temperature is uncalibrated. Therefore, the heat flux data computed from the surface temperature are not absolutely calibrated either. However, relative comparisons of heat flux profiles before and after the 3-D field application should be valid. The several kHz framing rate enables heat flux measurement of transient events, such as ELMs and disruptions. The fast framing rate also facilitates measurement of the formation of striations in the divertor heat flux footprints, which can start to appear within 3–4 ms after initiation of the 3-D field coil.

The D_α emission at the lower divertor target is recorded by a 1-D CCD camera installed at $\varphi = 255°$. It is operated at 2 kHz rate and with ~0.5 mm spatial resolution and is a part of a system of CCD arrays.[18] The derivation of ionization flux (used as a proxy to the particle flux) from the D_α measurement has been carried out in NSTX,[19] with an assumed S/XB coefficient (i.e., ionizations per photon) of 20 to convert photon flux to particle flux. This technique assumes that both the electron impact ionization and the excitation of the neutral atom take place in the same volume of ionizing plasma. Also, the divertor recycling coeffcient with Li has been estimated from the SOLPS modelling[20] to be $R \sim 0.92$, compared to $R \sim 0.98$ without Li. The outer midplane electron temperature and density at the separatrix for these plasmas are normally $T_{e,sep} = 40$–60 eV, $n_{e,sep} \sim 1e19$ m^{-3}.

III. DATA ANALYSIS AND INTERPRETATION

Figure 1 shows the temporal evolution of an ELM-free H-mode discharge, enabled with Li wall coatings, and with an $n = 3$ perturbation field applied. The L–H transition is indicated by the drop of divertor D_α emission at ~130 ms, and the H-mode was sustained until ~880 ms. The 3-D field perturbation was applied at 350, 550, and 800 ms with constant amplitude of -0.7 kA, on top of the static $n = 3$ error field correction current of 0.2 kA. The amplitude of the coil current is below the ELM triggering threshold. The line-average electron density continued to rise in the H-mode phase and did not appear to be affected by the 3-D field application.
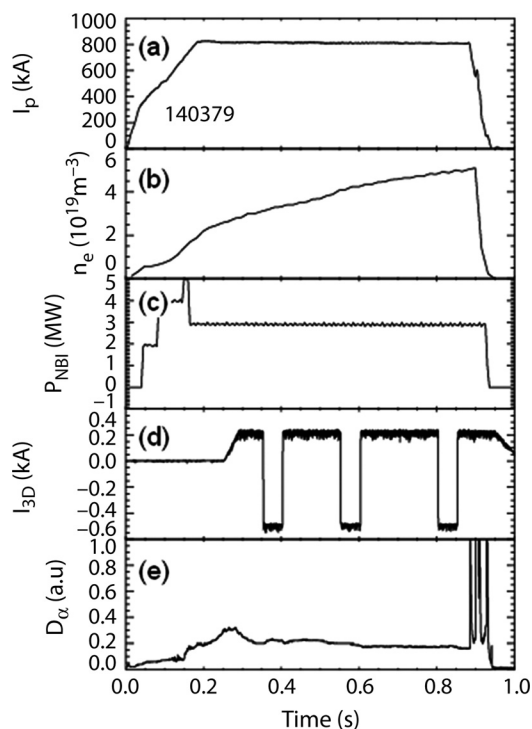

FIG. 1. Time evolution of various discharge parameters for a 3-D field applied shot: (a) plasma current, (b) line averaged density, (c) injected NBI power, (d) current in the external 3-D coil, (e) D_α signal for lower divertor. Note that the 3-D field coil was switched on at 350, 550, and 800 ms to -0.5 kA and lasted for 50 ms to give $n = 3$ perturbation field.

A. Breaking of axisymmetry of divertor heat and particle deposition by 3-D magnetic perturbation

The strike point splitting caused by the applied $n = 3$ magnetic perturbation is reflected as local peaks and valleys in the divertor heat flux profile and is measured by the IR camera. Figure 2 shows a comparison of the heat flux profile with a puncture plot from a field line tracing calculation, for the toroidal angle of the IR camera. It is seen that the main characteristics of the heat flux profiles do follow the vacuum field line tracing results, both in the number of the observed striations and in the relative spacing of the peaks. Some field lines for the split strike points originate from the pedestal region inside the separatrix and therefore have long connection lengths (see Fig. 6). They carry hotter and denser plasma particles and give higher heat and particle flux values to the divertor surface. This is why one can expect an agreement of the radial location of local peaks in the measured divertor profiles with that in the calculated connection length profile.

The inclusion of plasma response in an ideal perturbed equilibrium approach inside the unperturbed separatrix by the ideal perturbed equilibrium code (IPEC) calculation[21] did not affect the structure of split strike points significantly, i.e., the number and radial location of the generated lobes are unchanged relative to the vacuum field calculation (see Fig. 3). The B-field generated by the ideal plasma response up to a certain fraction of normalized poloidal flux (e.g., $\Psi_N = 0.97$) inside the separatrix is calculated by IPEC and is superposed to the vacuum field to begin field line tracing. Here, Ψ_N is defined as $\Psi_N = [\Psi_c - \Psi(r, z)]/(\Psi_c - \Psi_{sep})$, where Ψ_c is the poloidal
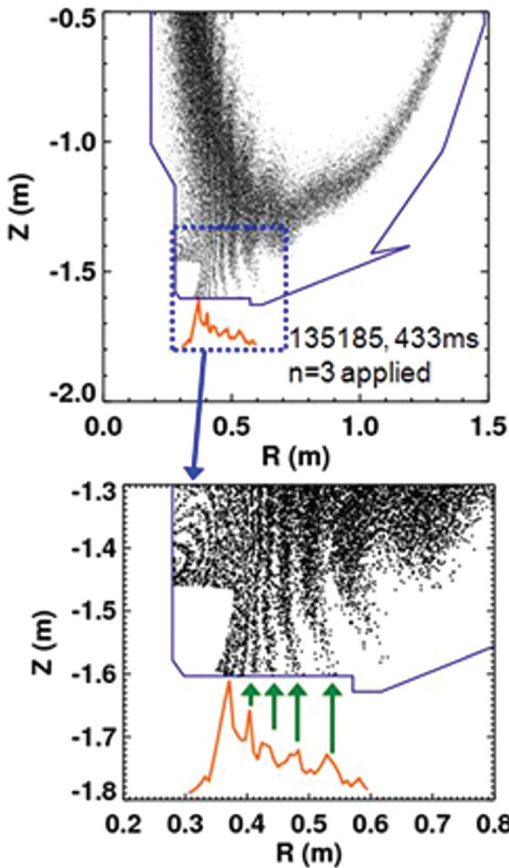
FIG. 2.   (Color online) Puncture plot of magnetic field lines for an $n=3$ perturbation application, calculated by a vacuum field line tracing code for the toroidal location of the IR camera at $\varphi = 135°$, with the measured heat flux profile overlaid. The statistical error bars on the measured heat flux are usually smaller than the size of the identified local peaks here.

flux at the magnetic centre and Ψ_{sep} is the flux at the separatrix. It is interesting to note that the intensity of the split strike points (the number of field lines in the lobes, crossing the poloidal plane in the puncture plot) becomes stronger if the ideal plasma response is included, but the envelope of the lobes does not change.
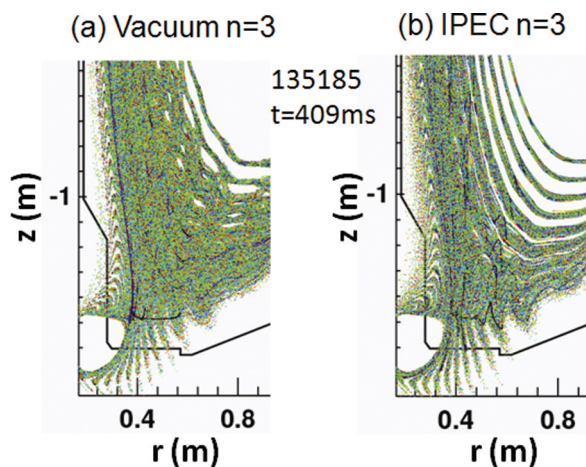

FIG. 3.   (Color online) Poloidal Poincare plot from a vacuum field line tracing calculation (a) and from the one with the ideal plasma response included in the field line tracing, up to 97% of normalized flux ($\Psi_N = 0.97$) inside the separatrix, calculated by IPEC (b).
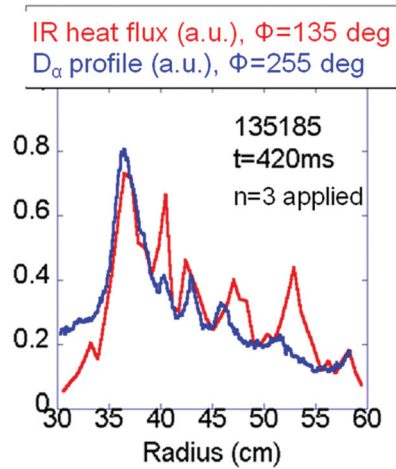

FIG. 4.   (Color online) Heat and particle flux profiles measured by IR and D_α cameras at different toroidal angles, $\varphi = 135°$ and $255°$, respectively.

The spatial structure of the measured heat flux and D_α profiles in the presence of $n=3$ magnetic perturbation is expected to be the same because of the $120°$ of toroidal displacement between the installed locations of the IR and D_α cameras, if the generated strike point splitting is consistent with the imposed $n=3$ fields. Indeed, the temporal and spatial evolution of striations is very similar for both the heat flux and D_α profiles, and Fig. 4 shows that the radial location of local peaks and valleys are similar in the two profiles. However, as is generally observed in NSTX, the amplitude of local peaks in the heat flux profile is larger than that in the D_α profile. A possible explanation for this may be that the heat source only comes from the plasma inside the separatrix so that the long connection length field lines carrying hotter plasma particles from the pedestal region easily make the local peaks more pronounced, while particle source comes both from the plasma and from the divertor recycling. With the recycling coefficient of 0.92 even with the use of Li, the particle influx from the pedestal region to the divertor surface for the split strike points should have been compensated by another influx from the divertor recycling. This addition could have raised the background level of the particle flux at the divertor surface, making the relative height of local peaks smaller compared to the heat flux profile.

Application of $n=1$ fields provides direct evidence of the generated toroidal asymmetry of the divertor profiles by the imposed fields. We have applied the $n=1$ fields at six different phase angles in the toroidal direction with one specific angle for each discharge. The phase angle was varied by $60°$ for the next discharge until the full toroidal coverage of $360°$ was completed for a total of six discharges. Figure 5 shows comparison of measured heat flux profiles for all of this discharges with six different phase angles of $n=1$ perturbation, i.e., from $30°$ through $330°$. It is seen that the location of local peaks, representing the split strike points, in the three profiles are clearly different from each other. This shows that the divertor heat deposition becomes toroidally asymmetric by the nonaxisymmetric magnetic perturbation. We have also compared the result of field line tracing to the measured divertor profiles and confirmed that the two results are in good agreement.
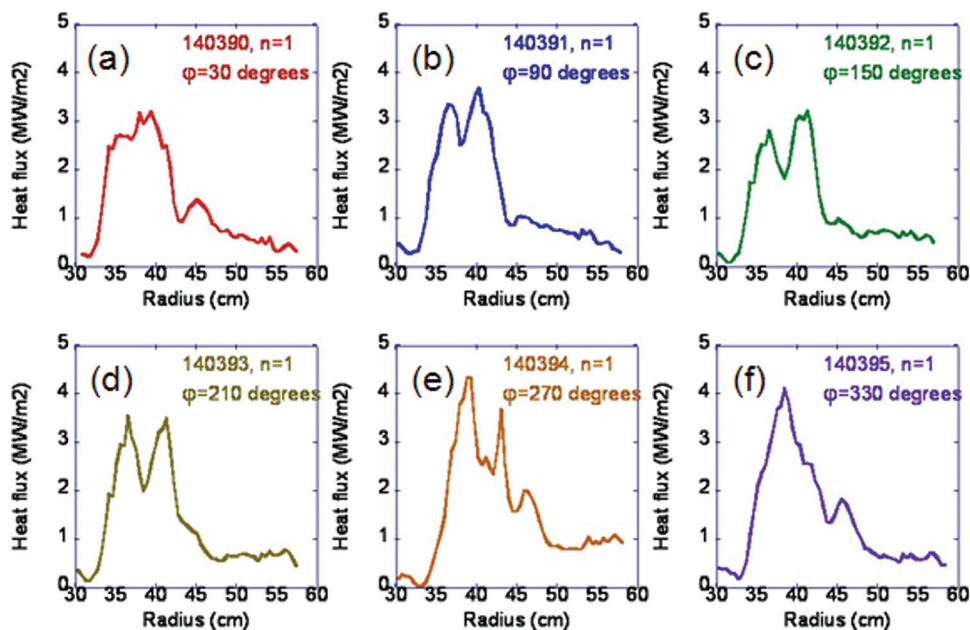
FIG. 5. (Color online) Measured heat flux profiles by the IR camera installed at the toroidal angle of 135°, for six different phase angles of the applied $n = 1$ magnetic perturbation, starting from 30° (a) to 330° (e) with increment of 60°.

The divertor profiles show a moderate level of strike point splitting even before the application of external magnetic perturbation in some high triangularity (δ) discharges.[5,22] The profiles show nearly monotonic decay, i.e., no strike point splitting, during the early stage of the discharge typically until $t \sim 200$ ms for the discharges chosen in this study and then begin to develop local peaks and valleys in the scrape-off layer region. The degree of splitting varies in time, and both the heat flux and the D_α profiles show similar evolution.[22] As a possible source of the 3-D magnetic perturbation, the intrinsic error field from the noncircularity of poloidal field coils was considered. It was recently shown[23] that the PF5 coil in NSTX produces error fields with $n = 3$ component as a dominant one. The inclusion of PF5 noncircularity in the vacuum field line tracing is therefore expected to produce a dominant $n = 3$ field structure although the model contains all noncircular components. Figure 6 shows a comparison of computed connection length profiles between the $n = 3$ application and the PF5 intrinsic error field cases; the radial locations of the local peaks are in good agreement. This indicates that intrinsic error fields may
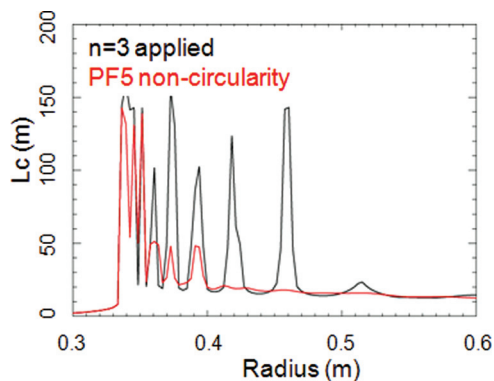
be one of the sources of the intrinsic strike point splitting. We therefore refer to this as "intrinsic strike point splitting" for the remainder of this paper. However, for some other discharges, intrinsic strike point splitting is not observed during the whole plasma duration time. It is observed that the temporal evolution of the intrinsic strike point splitting agrees reasonably well with that of the PF5 coil current amplitude above a certain value, i.e., higher PF5 coil current is associated with higher degree of intrinsic strike point splitting. This error field effect is presently not included in the field line tracing for the external 3-D fields application case. That is, we model either the $n = 3$ intrinsic error fields or the external $n = 3$ fields application, each alone. The inclusion of the error fields in the calculation of strike point splitting for the external 3-D field application is important for more accurate result. This is being pursued and we expect to be able to see the result in the near future.

B. Effect of parameter changes on the divertor profile modification with applied $n = 3$ fields; q_{95} and pedestal electron collisionality

The poloidal spectrum produced by the midplane coils is roughly fixed with the given coil geometry. Thus a scan of safety factor, q_{95}, was carried out by changing plasma current to look for the effect on the divertor profile modification. Field line tracing indicates that plasmas with higher q_{95} produce more striations than those with lower q_{95}. This is experimentally confirmed that the number of local peaks in D_α profile for a given radial range increases with increasing q_{95}, and comparison of the measured profile with the field line tracing shows good agreement for different q_{95}. The number of local peaks in the heat flux profile for a given radial range also increases with increasing q_{95} (from 8 to 11). Although the total number of peaks does not increase from $q_{95} = 11$ to $q_{95} = 15$, it is seen that the distance between local peaks for $r \geq 43$ cm becomes shorter for the higher q_{95} case. The D_α camera has excellent spatial resolution (~ 0.5 mm) and can
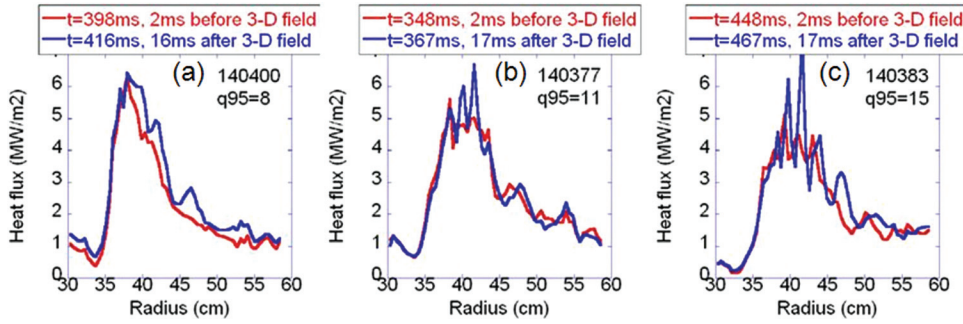

FIG. 6. (Color online) Comparison of computed connection length profiles between $n = 3$ field applied (black, higher peaks) and the PF5 intrinsic error field (red, lower peaks) cases.

FIG. 7. (Color online) Comparison of measured heat flux profiles before and after the 3-D fields application with varying q_{95}; (a) $q_{95} = 8$, (b) $q_{95} = 11$, (c) $q_{95} = 15$.

easily resolve narrow local peaks and valleys produced in the high q_{95} discharges, while the poorer spatial resolution of the IR camera (5–7 mm) may have been insufficient to resolve the finer striations in the heat flux profile for $r \leq 43$ cm for high q_{95} discharges. Another thing to note in the heat flux profile, in comparison with the profiles before the $n = 3$ perturbation was applied, is that higher fraction of the heat flux is carried through the split strike point channels in higher q_{95} cases (see Fig. 7). In other words, the local peaks in the profile become relatively higher with increasing q_{95}. On the other hand, the opposite is observed for the D_α profile, for which the reason is not yet clear.

The pedestal electron collisionality is also of interest for its impact on the divertor profiles because it is commonly believed that the field lines forming the strike point splitting originate from the pedestal region inside the separatrix and therefore the pedestal electron collisionality would directly affect the transport processes and subsequently the divertor profiles. The electron–electron collisionality, $v_{ee}^* = q_{95}R\varepsilon^{-3/2}\lambda_{ee}^{-1}$, where electron mean free path is given by $\lambda_{ee} = v_{th}\tau_{ee} \propto (T_e^2/n_e \ln \Lambda)$, is directly affected by the pedestal electron temperature and density. We attempted to change the pedestal T_e by changing the neutral beam injection (NBI) beam power (2–6 MW) and the n_e by taking data at different time slices during the density ramp-up period for the ELM-free H-mode plasmas (see Fig. 1). Although NSTX has somewhat limited response of the pedestal T_e and n_e to the heating power and the line averaged density $\bar{n}_e$, respectively, we were able to achieve the v_{ee}^* variation by up to a factor of ~ 3 by simultaneously varying the heating power and the line averaged density. The estimated pedestal collisionality $(2 < v_{ee}^* < 6)$ is significantly higher than the ITER-relevant low collisionality $(v_{ee}^* \sim 0.2)$. The left plot in Fig. 8 shows the pedestal collisionality against the pedestal T_e, both at the location of 95% of the normalized flux Ψ_N. The middle and right plots show the D_α profiles for the high and low colli-

sionalities with the same amplitude of $n = 3$ fields applied. Note that the local peaks in the D_α profile becomes more pronounced for higher collisionality. This is consistent with the previous result[3] that the strike point splitting was only observed in higher pedestal collisionalities, i.e., $v_{ee}^* > 0.5$. However, the heat flux profile does not show a noticeable difference for the range of collisionality variation in this work. This might be due to the difference between the heat and particle transport processes, but more data analysis are certainly needed for clearer conclusion. A thorough 3-D transport simulation would also help to clarify this issue.

C. Heat flux deposition during ELMs triggered by applied 3-D fields

Externally imposed 3-D fields with sufficient amplitude trigger ELMs and strong heat and particle expulsion to the divertor plates.[9,22] The frame speed of our IR camera in this work was sufficient (1.6–3.8 kHz) to resolve heat flux profiles during the ELM. Plot (a) in Fig. 9 shows the calculated heat flux profiles at the ELM peak and immediately (0.7 ms) before the ELM occurrence in case of $n = 3$ application. Loss of around $\sim 8\%$ of total energy from the plasma core due to the triggered ELM burst is observed. Notice that the strike point splitting is persistent even during the ELM $(t = 376.7 \text{ ms})$ as the profile exhibits local peaks and valleys. Also, the radial location of the split strike points before and during the ELM agrees. This indicates that the heat flux profile from ELMs triggered by $n = 3$ fields follows the imposed field structure. In other words, the spatial heat deposition during the triggered ELMs is phase locked to the external 3-D fields. This is the same result as was previously seen in DIII-D (Ref. 4) for the $n = 3$ field application. Plot (b) in Fig. 9 shows the heat flux profiles across an ELM is triggered by an $n = 1$ field application ($\sim 9\%$ of total energy loss is observed due to the ELM burst), showing a noticeable
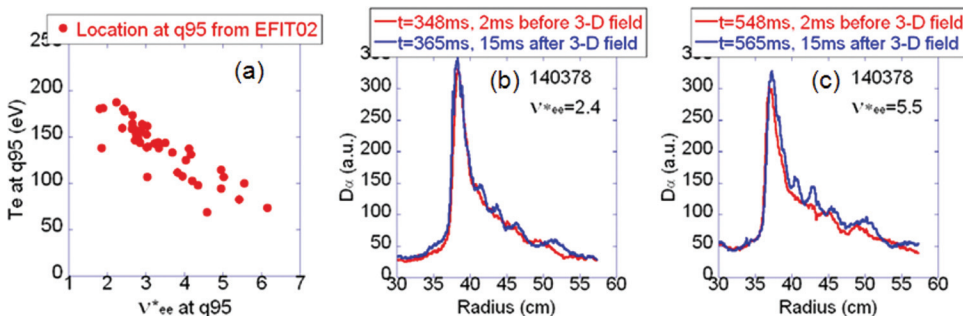

FIG. 8. (Color online) Estimated pedestal electron collisionality against the pedestal T_e (a). Comparison of D_α profiles before and after the 3-D fields application for low (b) and high (c) collisionalities.
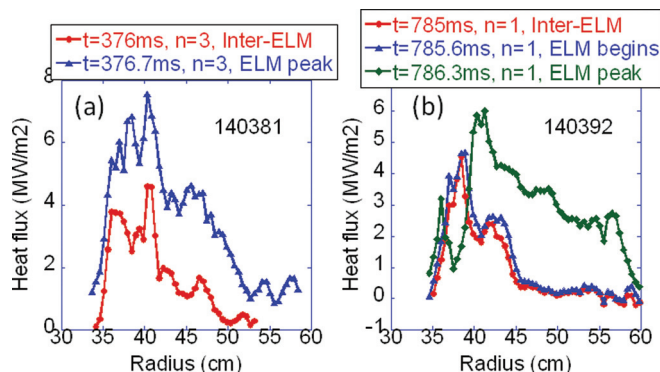
FIG. 9. (Color online) Measured heat flux profiles before and after an ELM occurrence with $n = 3$ (a) and $n = 1$ (b) fields applied.
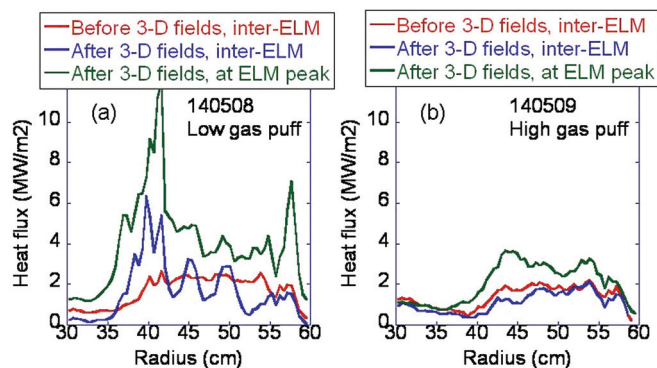

FIG. 10. (Color online) Measured heat flux profiles before (red, upper legend) and after (blue, middle legend, inter-ELM; green, lower legend, ELM peak) the 3-D field application. Plot (a) is for the detached divertor plasma with lower gas puffing and plot (b) is with higher gas puffing.

discrepancy between the spatial structure of the profiles before and during the ELM. This data indicates that the phase locking of the ELM heat deposition to the imposed 3-D field structure is limited to the $n = 3$ application case. As the observation of local peaks in the heat flux profile is the end product of the toroidal structure of the applied 3-D fields and the triggered ELMs, it is not possible to deconvolve one from the other with our data alone. We would need to simulate a higher-n ELM with low-n magnetic perturbation, to see what mode number pattern is produced.

D. Effect of 3-D fields on the divertor detachment

As ITER considers to employ external coil sets to apply 3-D fields for the ELM suppression and also will need to maintain the divertor detachment for the mitigated heat flux to the divertor surface, it is of high importance to understand how 3-D fields affect the detached divertor plasma. This investigation is difficult in other devices because of the low line averaged density caused by the density pump out during the 3-D field application. As there is no density pump out during the 3-D field application in NSTX, it is possible to raise the divertor density and investigate the impact of 3-D fields on the divertor detachment. Their impact on the naturally occurring ELMs has been also investigated with the divertor plasma collisionality varied by the deuterium divertor gas puffing. As more gas is puffed into the divertor area, the plasma becomes more collisional and the divertor plasma changes from the attached to the partially detached regime. This is the same as the previously observed results.[24,25] The divertor detachment also tends to reduce the ELM size as the pedestal temperature and density decreases with increasing gas puffing.. As the maximum tolerable size of the ELM in ITER is generally referred to as 1% of the pedestal stored energy, we attempted to reduce the ELM size as much as possible to apply $n = 3$ fields. As the divertor gas puffing rate increases, the plasma became increasingly detached and this resulted in a flattened profile with a lower heat flux. Surprisingly, the application of $n = 3$ fields brought the detached divertor plasma back to the attached regime at the divertor gas puffing rate of 2000 Torr. This is indicated by the peaked heat flux profile (inter-ELM period, blue curve) in the left plot of Fig. 10. For this puffing rate, the ELMs were strong enough to burn through the detachment and produced highly

peaked heat flux profile (at the ELM peak), i.e., ELMs reattach the detached plasma, irrespective of the 3-D field application. Note that the inter-ELM heat flux profile has multiple local peaks representing the strike point splitting generated by the imposed 3-D fields. When an ELM hit the divertor surface in the presence of 3-D fields, the heat flux profile rises significantly with the location of local peaks staying the same as in the inter-ELM profile. The reattachment of the divertor plasma during the inter-ELM period can be overcome with additional gas puffing. The right plot of Fig. 10 shows that the plasma stays in the detached regime before and after the 3-D field application (inter-ELM period, red and blue curves) at the gas puffing rate of 3000 Torr. The ELM did not induce the reattachment either, it only increased the whole heat flux level by a factor of ~ 2 with the flattened profile shape unchanged (green curve), an important signature of the divertor detachment. It is not deconvolvable whether the detachment during the ELM is due to the 3-D fields or just because of the high gas puffing rate. However, the sustainment of detachment during the inter-ELM period in the presence of 3-D fields for high gas puff rate is potentially important for the future device such as ITER because the use of 3-D magnetic perturbations must be compatible with the divertor detachment as well as other favorable plasma regimes.

IV. SUMMARY AND CONCLUSIONS

The applied 3-D fields modify divertor heat and particle flux profiles in a manner consistent with vacuum field line tracing. The inclusion of ideal plasma response inside the separatrix in the field line tracing does not significantly change the radial location and spacing of split strike points. This is important because it suggests that vacuum field line tracing may be sufficient to predict the structure of the generated strike point splitting under certain conditions. Measurements taken for different phase angles of the applied $n = 1$ perturbation fields provide the most direct evidence of the breaking of toroidal axisymmetry of the divertor profiles. The noncircularity of PF5 coil was modelled to be included in the vacuum field line tracing and was shown to generate similar field structure to the case of $n = 3$ field application. This indicates that the intrinsic error fields are one of the

causes of the intrinsic strike point splitting observed in divertor profiles for some NSTX discharges. Heat flux profiles measured at the peak of the triggered ELMs by $n = 3$ perturbation fields show that the structure of split strike points is persistent even during the ELMs and the heat flux follows the imposed field structure. However, results for $n = 1$ perturbation show cases that the ELM heat flux does not follow the externally applied field structure. Investigation of more ELM heat flux data triggered by $n = 1$ fields as well as a simulation of higher n-number ELMs with lower-n 3-D fields is necessary to draw a clearer conclusion for the spatial structure of the triggered ELMs.

q$_{95}$ and plasma collisionality have been varied to examine their impact on the divertor profiles. It was revealed that the split strike points become more and finer for higher q$_{95}$ and the fraction of heat flowing through this split channels increases with increasing q$_{95}$. An opposite trend is observed for the fraction of particle flux, i.e., from the D$_\alpha$ profile. As collisionality is believed to play an important role in the transport processes governing the striations in the divertor profiles, the pedestal electron collisionality was varied by simultaneously changing the NBI power and choosing time slices at different line averaged densities in order to change the pedestal T_e and n_e, respectively. The estimated electron collisionality was quite high ($2 < v_{ee}^* < 6$), and it was not possible to achieve v_{ee}^* lower than 2. This collisionality range may have been too high for a significant difference in the amplitude of local peaks in the heat flux profile to occur, but the D$_\alpha$ profile showed a noticeable difference, i.e., higher amplitude of local peaks for the higher collisionality. A 3-D transport simulation will be needed to elucidate the underlying physics.

The applied 3-D fields are found to induce the reattachment of detached plasma with lower divertor gas puffing rate, but additional gas puffing allowed to keep the detachment in the presence of external 3-D fields. In this condition, heat flux profile even at the ELM peak stayed mitigated and flattened, a signature of continued divertor detachment. Study is underway to clarify if the reattachment by the applied 3-D fields is accompanied by the altered pedestal profile or it is solely a phenomenon occurring in the divertor region.

ACKNOWLEDGMENTS

[1]R. J. Buttery, T. C. Hender, J. D. Ashall, K. B. Axon, G. Blow, and S. J. Fielding, Nucl. Fusion **36**, 1369 (1996).

[2]T. E. Evans, R. K. W. Roeder, J. A. Carter, B. I. Rapoport, M. E. Fenstermacher, and C. J. Lasnier, J. Phys.: Conf. Ser. **7**, 174 (2005).

[3]O. Schmitz, T. E. Evans, M. E. Fenstermacher, H. Frerichs, M. W. Jakubowski, M. J. Schaffer, A. Wingen, W. P. West, N. H. Brooks, K. H. Burrell, J. S. deGrassie, Y. Feng, K. H. Finken, P. Gohil, M. Groth, I. Joseph, C. J. Lasnier, M. Lehnen, A. W. Leonard, S. Mordijck, R. A. Moyer, A. Nicolai, T. H. Osborne, D. Reiter, U. Samm, K. H. Spatschek, H. Stoschus, B. Unterberg, E. A. Unterberg, J. G. Watkins, R. Wolf, and the DIII-D and TEXTOR Teams, Plasma Phys. Controlled Fusion **50**, 124029 (2008).

[4]M. W. Jakubowski, T. E. Evans, M. E. Fenstermacher, M. Groth, C. J. Lasnier, A. W. Leonard, O. Schmitz, J. G. Watkins, T. Eich, W. Fundamenski, R. A. Moyer, R. C. Wolf, L. B. Baylor, J. A. Boedo, K. H. Burrell, H. Frerichs, J. S. deGrassie, P. Gohil, I. Joseph, S. Mordijck, M. Lehnen, C. C. Petty, R. I. Pinsker, D. Reiter, T. L. Rhodes, U. Samm, M. J. Schaffer, P. B. Snyder, H. Stoschus, T. Osborne, B. Unterberg, E. Unterberg, and W. P. West, Nucl. Fusion **49**, 095013 (2009).

[5]J-W. Ahn, J. M. Canik, V. A. Soukhanovskii, R. Maingi, and D. J. Battaglia, Nucl. Fusion **50**, 045010 (2010).

[6]T. E. Evans, R. A. Moyer, K. H. Burrell, M. E. Fenstermacher, I. Joseph, A. W. Leonard, T. H. Osborne, G. D. Porter, M. J. Schaffer, P. B. Snyder, P. R. Thomas, J. G. Watkins, and W. P. West, Nature Phys. **2**, 419 (2006).

[7]Y. Liang, H. R. Koslowski, P. R. Thomas, E. Nardon, S. Jachmich, A. Alfier, G. Arnoux, Y. Baranov, M. Becoulet, M. Beurskens, R. Coelho, Th. Eich, E. De La Luna, W. Fundamenski, S. Gerasimov, C. Giroud, M. P. Gryaznevich, D. Harting, A. Huber, A. Kreter, L. Moreira, V. Parail, S. D. Pinches, S. Saarelma, O. Schmitz, and JET-EFDA Contributors, Nucl. Fusion **50**, 025013 (2010).

[8]A. Kirk, E. Nardon, R. Akers, M. Bécoulet, G. De Temmerman, B. Dudson, B. Hnat, Y. Q. Liu, R. Martin, P. Tamain, D. Taylor, and the MAST Team, Nucl. Fusion **50**, 034008 (2010).

[9]J. M. Canik, R. Maingi, T. E. Evnas, R. E. Bell, S. P. Gerhardt, H. W. Kugel, B. P. LeBlanc, J. Manickam, J. E. Menard, T. H. Osborne, J.-K. Park, S. Paul, P. B. Snyder, S. A. Sabbagh, E. A. Unterberg, and the NSTX Team, Nucl. Fusion **50**, 034012 (2010).

[10]R. Maingi, T. H. Osborne, B. P. LeBlanc, R. E. Bell, J. Manickam, P. B. Snyder, J. E. Menard, D. K. Mansfield, H.W. Kugel, R. Kaita, S. P. Gerhardt, S. A. Sabbagh, F. A. Kelly, and the NSTX Research Team, Phys. Rev. Lett. **103**, 075001 (2009).

[11]J. M. Canik, R. Maingi, T. E. Evnas, R. E. Bell, S. P. Gerhardt, B. P. LeBlanc, J. Manickam, J. E. Menard, T. H. Osborne, J.-K. Park, S. F. Paul, P. B. Snyder, S. A. Sabbagh, H. W. Kugel, E. A. Unterberg, and the NSTX Team, Phys. Rev. Lett. **104**, 045001 (2010).

[12]S. A. Sabbagh, R. E. Bell, J. E. Menard, D. A. Gates, A. C. Sontag, J. M. Bialek, B. P. LeBlanc, F. M. Levinton, K. Tritz, and H. Yuh, Phys. Rev. Lett. **97**, 045004 (2006).

[13]J. E. Menard, M. G. Bell, R. E. Bell, S. Bernabei, J. Bialek, T. Biewer, W. Blanchard, J. Boedo, C. E. Bush, M. D. Carter, W. Choe, N. A. Crocker, D. S. Darrow, W. Davis, L. Delgado-Aparicio, S. Diem, C. W. Domier, D. A. D'Ippolito, J. Ferron, A. Field, J. Foley, E. D. Fredrickson, D. A. Gates, T. Gibney, R. Harvey, R. E. Hatcher, W. Heidbrink, K. W. Hill, J. C. Hosea, T. R. Jarboe, D. W. Johnson, R. Kaita, S. M. Kaye, C. E. Kessel, S. Kubota, H. W. Kugel, J. Lawson, B. P. LeBlanc, K. C. Lee, F. M. Levinton, N. C. Luhmann, Jr., R. Maingi, R. P. Majeski, J. Manickam, D. K. Mansfield, R. Maqueda, R. Marsala, D. Mastrovito, T. K. Mau, E. Mazzucato, S. S. Medley, H. Meyer, D. R. Mikkelsen, D. Mueller, T. Munsat, J. R. Myra, B. A. Nelson, C. Neumeyer, N. Nishino, M. Ono, H. K. Park, W. Park, S. F. Paul, T. Peebles, M. Peng, C. Phillips, A. Pigarov, R. Pinsker, A. Ram, S. Ramakrishnan, R. Raman, D. Rasmussen, M. Redi, M. Rensink, G. Rewoldt, J. Robinson, P. Roney, A. L. Roquemore, E. Ruskov, P. Ryan, S. A. Sabbagh, H. Schneider, C. H. Skinner, D. R. Smith, A. Sontag, V. Soukhanovskii, T. Stevenson, D. Stotler, B. C. Stratton, D. Stutman, D. Swain, E. Synakowski, Y. Takase, G. Taylor, K. Tritz, A. von Halle, M. Wade, R. White, J. Wilgen, M. Williams, J. R. Wilson, H. Yuh, L. E. Zakharov, W. Zhu, S. J. Zweben, R. Akers, P. Beiersdorfer, R. Betti, T. Bigelow, M. Bitter, P. Bonoli, C. Bourdelle, C. S. Chang, J. Chrzanowski, L. Dudek, P. C. Efthimion, M. Finkenthal, E. Fredd, G. Y. Fu, A. Glasser, R. J. Goldston, N. L. Greenough, L. R. Grisham, N. Gorelenkov, L. Guazzotto, R. J. Hawryluk, J. Hogan, W. Houlberg, D. Humphreys, F. Jaeger, M. Kalish, S. Krasheninnikov, L. L. Lao, J. Lawrence, J. Leuer, D. Liu, G. Oliaro, D. Pacella, R. Parsells, M. Schaffer, I. Semenov, K. C. Shaing, M. A. Shapiro, K. Shinohara, P. Sichta, X. Tang, R. Vero, M. Walker, and W. Wampler, Nucl. Fusion **47**, S645 (2007).

[14]J-W. Ahn, R. Maingi, D. Mastrovito, and A. L. Roquemore, Rev. Sci. Instrum. **81**, 023501 (2010).

[15]S. P. Gerhardt, J. E. Menard, J.-K. Park, R. Bell, D. A. Gates, B. P. LeBlanc, S. A. Sabbagh, and H. Yuh, Plasma Phys. Controlled Fusion **52**, 104003 (2010).

[16]A. G. McLean, "A dual-band adaptor for infrared imaging," to be submitted to Rev. Sci. Instrum.

[17]A. Herrmann, W. Junker, K. Gunther, S. Bosch, M. Kaufmann, J. Neuhauser, G. Pautasso, Th. Richter, R. Schneider, and ASDEX-Upgrade Team, Plasma Phys. Controlled Fusion **37**, 17 (1995).

[18]V. A. Soukhanovskii, A. L. Roquemore, C. H. Skinner, J. Menard, H. W. Kugel, D. Johnson, R. Maingi, S. Sabbagh, and F. Paoletti, Rev. Sci. Instrum. **74**, 2094 (2003).

[19] V. A. Soukhanovskii, R. E. Bell, C. Bush, R. Kaita, H. W. Kugel, B. P. LeBlanc, R. Maingi, R. Raman, A. L. Roquemore, and NSTX Research Team, J. Nucl. Mater. **390–391**, 516 (2009).

[20] J. M. Canik, R. Maingi, V. A. Soukhanovskii, R. E. Bell, H. W. Kugel, B. P. LeBlanc, and T. H. Osborne, J. Nucl. Mater. (2011).

[21] J.-K. Park, A. H. Boozer, and A. H. Glasser, Phys. Plasmas **14**, 052110 (2007).

[22] J-W. Ahn, J. M. Canik, R. Maingi, T. K. Gray, J. D. Lore, A. G. McLean, J.-K. Park, A. L. Roquemore, and V. A. Soukhanovskii, J. Nucl. Mater. (2011).

[23] J. E. Menard, R. E. Bell, D. A. Gates, S. P. Gerhardt, J.-K. Park, S. A. Sabbagh, J. W. Berkery, A. Egan, J. Kallman, S. M. Kaye, B. LeBlanc, Y. Q. Liu, A. Sontag, D. Swanson, H. Yuh, W. Zhu, and the NSTX Research Team, Nucl. Fusion **50**, 045008 (2010).

[24] T. W. Petrie, R. Maingi, S. L. Allen, D. A. Buchenauer, D. N. Hill, and C. J. Lasnier, Nucl. Fusion **37**, 643 (1997).

[25] V. A. Soukhanovskii, R. Maingi, D. A. Gates, J. E. Menard, S. F. Paul, R. Raman, A. L. Roquemore, R. E. Bell, C. E. Bush, R. Kaita, H. W. Kugel, B. P. LeBlanc, D. Mueller, and the NSTX Team, Nucl. Fusion **49**, 095025 (2009).